Revision 2:

Nanostructure reveals REE mineral crystallization mechanisms in granites from heavy-REE deposit, South China

AIGUO SHI[1], CHENG XU[1,2*], ANTON R. CHAKHMOURADIAN[3], MARTIN P. SMITH[4], JINDRICH KYNICKY[5], CHAOXI FAN[1], CHUNWAN WEI[1], AND GUANGXI KUANG[1]

[1]Key Laboratory of Orogenic Belts and Crustal Evolution, School of Earth and Space Sciences, Peking University, Beijing 100871, China.

[2]College of Earth Sciences, Guilin University of Technology, Guilin 540001, China.

[3]Department of Geological Sciences, University of Manitoba, Winnipeg, MB R3T2N2, Canada.

[4]School of Environment and Technology, University of Brighton, Brighton BN24GJ, UK.

[5]BIC Brno, Technology Innovation Transfer Chamber, Brno 61200, Czech Republic.

*Email: xucheng1999@pku.edu.cn

ABSTRACT

Weathering crusts after granites are the most important source of heavy rare-earth elements (HREE) worldwide. Although HREE in these deposits are known to be inherited from parental rocks, the origin of HREE enrichment and reasons why it is rare outside of China remain unclear. Here, we report the occurrence of variably organized nanoparticles of Ce-poor (<0.2 wt.%), Nd-Y-rich bastnäsite-(La) and associated cerianite in parental granites from a HREE deposit, South China. The mineral contains high HREE abundances (up to 13 wt.% Y_2O_3). Synchrotron radiation-induced X-ray diffraction and high-resolution transmission electron microscopy analyses suggest that the mineral grew as disordered nanocrystals, and coaligned, or nearly coaligned nanoparticle aggregations, thus supporting “nonclassical” crystallization mechanisms by particle attachment under hydrothermal conditions. The nanocrystalline Ce-poor, Nd-Y-rich bastnäsite-(La) precipitated at rapidly decreasing temperature related to the influx of externally derived fluids, which caused CO_2-H_2O immiscibility and REE supersaturation. This interpretation is supported by petrographic data and microthermometric analysis of fluid inclusions in quartz. Unusually high $f(O_2)$ resulted in Ce oxidation and decoupling from trivalent lanthanides, producing polycrystalline mineralization, which decomposed easily during late weathering stages to release HREE.

Keywords: Ce-poor and Nd-Y-rich bastnäsite-(La), nanoparticles, crystallization by particle attachment, oxygen fugacity, REE deposits, South China granite

INTRODUCTION

The rare-earth elements (REE), generally defined as the lanthanides plus yttrium (Y), are considered critical raw materials because of their extensive applications in renewable energy solutions and modern technologies (Kalvig and Machacek 2018). Recently, concerns over the perceived imbalance between the increasing demand for these resources and their supply shortages have led to a surge in REE exploration worldwide, since China, the largest REE producer in the past 30 years, reduced its REE export quota (Gulley et al. 2018). Heavy REE (HREE = Gd-Lu + Y) are much less abundant than light REE (LREE = La-Eu) and are anticipated to be associated with the highest supply risk in the foreseeable future (Balaram 2019). The majority of economically exploitable HREE resources are associated with regolith-hosted ion-adsorption deposits (IAD) in South China (Martin et al. 2020). The HREE are adsorbed as ionic complexes onto clay minerals in weathering crusts developed over igneous, mostly granitoid rocks (Bao et al. 2008). These deposits account for about 80% of the global HREE supply (Bernhardt and Reilly 2020). The forms of REE adsorption on clays reported to date primarily

include readily leachable eightfold- to ninefold-coordinated outer-sphere hydrated complexes, which are dominantly attached to the clays kaolinite and halloysite (Borst et al. 2020). Although weathering of granitoids under warm and humid conditions plays an important role in REE fractionation and enrichment, this process is expected to yield high LREE/HREE ratios in IAD because LREE are hosted in phases relatively more susceptible to weathering in comparison with HREE-enriched phases (Estrade et al. 2019; Prameswara et al. 2021). Geologically similar IAD were identified elsewhere in Southeast Asia (Sanematsu et al. 2013) and Madagascar (Janots et al. 2015), and these deposits generally exhibit stronger enrichment in LREE than HREE. The extent of relative enrichment and fractionation among leachable REE is believed to be controlled by the nature of the precursor bedrock and REE-hosting minerals in that rock (Martin et al. 2017; Estrade et al. 2019). Therefore, one essential question that needs to be addressed to understand the origin of IAD is how HREE-rich minerals form in their precursor granitoid rocks.

Xu et al. (2017) reported three types of previously unidentified, Ce-poor, LREE- and HREE-enriched minerals in the South China granites. The weathering profiles inherited the REE signature of their parental granites, reflecting the depletion in Ce and enrichment in both LREE and HREE. Different horizons within the weathering profile show variable enrichment

levels in LREE and HREE. Uncommon REE minerals were interpreted to have served as the principal source of HREE incorporated in the mineralized weathering crusts (Xu et al. 2017); however, the exact nature and genesis of these minerals were not very clear. Understanding their origin and paragenetic role in the parental granites has become a priority in explaining why HREE-rich clays are particularly abundant in South China. This work also has practical implications for mineral exploration as it provides criteria for the identification of similar HREE-rich IAD elsewhere. Here, we report unusual nanostructures observed in a Ce-poor, REE fluorocarbonate mineral [referred to hereafter as Ce-poor, Nd-Y-rich bastnäsite-(La)] from the Zhaibei granites, which weathered to give rise to the famous HREE deposits of South China (also known as “South China clays”). Our results provide evidence for a crystallization mechanism novel among REE minerals, which involves crystal growth by oriented and disoriented attachment of nanoparticles, and further supports the idea that HREE enrichment in the parental granites was related to rapid crystallization in a highly oxidized environment.

GEOLOGICAL BACKGROUND

Vast quantities of granitic rocks, associated with subordinate gabbros and basalts, were emplaced in the South China Block during the Mesozoic. Mao et al. (2008) suggested that these rocks were products of three episodes of

magmatic activity: Late Triassic (230-210 Ma), Middle-Late Jurassic (170-150 Ma), and Early Cretaceous (134-90 Ma). The Early Mesozoic intrusions were confined mostly to intracontinental areas, whereas the Cretaceous granites were distributed mainly towards the South China Sea coast (Fig. 1). Many studies identified subduction of the Paleo-Pacific plate beneath the Eurasian plate as responsible for the Mesozoic granitic magmatism in the region (Li and Li 2007; Zhou et al. 2006; Zhou et al. 2015). The Triassic episode produced voluminous S-type granites with high modal contents of Al silicates, in particular muscovite, garnet, and tourmaline (Wang et al. 2013). Jurassic granites are widespread in the Nanling region and primarily composed of biotite and two-mica varieties. These rocks include calc-alkaline I-type, alkaline A-type, and subordinate S-type granites (Zhou et al. 2015). Cretaceous granites are mostly of A- and I-types, and tend to occur closer to the coast (Sun et al. 2015).

Ore deposits are quite abundant in the South China granitic belt and include W, Sn, Sb, Bi, Cu, Pb, Zn, Nb, Ta, and REE targets. More than 90% of the HREE-rich IAD are located in Jiangxi, Guangdong and Guangxi provinces (Fig. 1). The examined weathering profiles in Zhaibei, southern Jiangxi, have a thickness ranging from 5 to 30 m, and are developed after Middle-Jurassic peraluminous biotite and muscovite granites (Li et al. 2003; Wang et al. 2015). The mineralized laterites show moderate LREE enrichment levels and

127 negative Ce and Eu anomalies; their REE budget (215-1334 ppm) is made up
128 of ~30-50% HREE (57-542 ppm; Xu et al. 2017). The Jurassic (188 Ma; Xu et
129 al. 2017) granites intruding Paleozoic granitoids have intrusive contacts with
130 Jurassic volcanic rocks in the western part of the study area, and are
131 separated by a fault from Cambrian metamorphic rocks in its northern part.
132 The parental rock of the Zhaibei REE-rich clays is medium- to coarse-grained
133 and composed of alkali feldspar (25-30%), plagioclase (25-32%), quartz
134 (30-35%), biotite (3-10%), and muscovite (< 2%) (Online Material[1] Fig. S1).
135 The accessory mineral assemblage includes REE phases, zircon, fluorapatite,
136 magnetite and ilmenite. The REE minerals are represented by monazite-(Ce),
137 xenotime-(Y), Ca-REE fluorocarbonates, allanite-(Ce), cerianite-(Ce) and
138 three HREE-rich minerals described in our earlier work as “REE-1, 2, 3” (Xu et
139 al. 2017). Both REE-1 and REE-2 apparently formed by alteration of
140 fluorapatite, which is highly susceptible to fluid-induced chemical and textural
141 changes under natural and experimental conditions (Fig. 2a; Harlov and
142 Förste 2003; Harlov 2015; Chakhmouradian et al. 2017). The Ce-poor,
143 Nd-Y-rich bastnäsite-(La) (“REE-3”) occurs as fracture fillings in feldspar.
144 Disseminated anhedral grains, up to 200 μm in size, developed interstitially to
145 quartz, biotite and feldspar (Fig. 2b, c). Cavities/vugs in samples contain thin
146 encrustations of Ce-poor, Nd-Y-rich bastnäsite-(La) lining the cavities (Fig. 2c).
147 This mineral did not form at an early stage of the weathering event, and is in

direct contact with biotite, quartz, and feldspar, or separated from them by a rim of unidentified hydrous Al-Fe-rich silicate (Fig. 2c, d) in the fresh parental rock. Cerianite veinlets are observed in the granite, where they are intimately intergrown with an unidentified hydrous Al-Fe-rich silicate (Fig. 2e). Ilmenite in this granite was partially converted to hematite, which was confirmed by Raman microspectroscopy (Fig. 2f and Online Material[1] Fig. S2).

ANALYTICAL METHODS

Mineral analysis

The major-element compositions of mineral phases in the granites were analyzed by wavelength-dispersive X-ray spectrometry (WDS) using a JEOL JXA-8230 electron microprobe at the East China University of Technology, Nanchang, China. According to the chemical composition and grain size of the individual minerals, each of them was analyzed with a set of appropriate matrix-specific standards (both natural and synthetic) and optimized instrumental conditions (detector type, beam settings, and counting statistics). The standards used during WDS analyses included sanidine (Si, K), plagioclase (Ca), rutile (Ti), magnetite (Fe), rhodonite (Mn), fluorite (F), jadeite (Na, Al), apatite (P), biotite (Mg), metallic Nb and Ta (Nb, Ta), uraninite (Th, U, Pb), monazite (La, Ce, Pr, Nd), and synthetic REE phosphates (Y, Sm, Eu, Gd, Dy, Ho, Er, Tm, Yb). The measurements were performed at an accelerating

voltage of 15 kV and a beam current of 20 nA, with an electron beam ranging 1-5 μm in diameter. For the analysis, Kα analytical lines were used for all elements except La, Ce, Pr, Nd, Nb, and Ta (Lα lines for all), and Sm (Lβ line). For REE-bearing minerals, raw WDS data were corrected using empirical interference values for REE and other elements potentially interfering with the REE signals, from well-characterized synthetic glass and phosphate standards. All raw data were corrected with standard ZAF correction procedures. Repeated analysis of the standards showed that the precision of the WDS measurements was ±2 % or better for most elements.

Synchrotron radiation-induced X-ray diffraction (SR-XRD)

In-situ SR-XRD analysis of Ce-poor, Nd-Y-rich bastnäsite-(La) was performed on polished thin sections at the 4W2 beamline of Beijing Synchrotron Radiation Facility, Beijing, China. The wavelength of the monochromatic X-ray beam was 0.6199 Å and the beam size was 20 × 30 μm^2. During the measurement, the silicate minerals surrounding Ce-poor, Nd-Y-rich bastnäsite-(La) were covered with a copper sheet with a hole 150 μm in diameter, which is close to the size of the analyzed fluorocarbonate grains. The thin section was continuously rotated from -20° to 20° about the X-ray beam axis at ambient conditions, and the collecting time was 300 s. The X-ray diffraction (XRD) patterns were acquired using an image plate detector

(MAR-345), calibrated with a CeO_2 standard, and then integrated to generate conventional one-dimensional profiles using the Fit2D program (Hammersley 1997).

High-resolution transmission electron microscopy (HRTEM)

Electron-transparent foils of representative Ce-poor, Nd-Y-rich bastnäsite-(La) grains for HRTEM analysis were prepared using the focused ion beam technique (FIB, Online Material[1] Fig. S3) on a Zeiss Auriga Compact dual beam instrument equipped with an Omniprobe AutoProbe 200 micromanipulator at the Institute of Geology and Geophysics, Chinese Academy of Sciences, Beijing, China. Final thinning and polishing were done using an ion beam at a voltage of 5-30 kV and beam current of 0.05-2 nA. The FIB section was ~100 nm in thickness. HRTEM images of the foils were obtained with an aberration-corrected scanning transmission electron microscope (FEI Titan Cubed Themis G2 300 at Peking University, Beijing, China), which was operated at an accelerating voltage of 300 kV and a beam current of ~2 nA. In addition, high-angle annular dark-field (HAADF) scanning transmission electron microscopy images and energy-dispersive X-ray spectroscopy (EDS) maps were recorded at an accelerating voltage of 300 kV and beam currents of ~50 pA and ~100 pA, respectively (Rice et al. 1990). EDS analyses were done in scanning transmission electron microscopy

(STEM) mode to avoid mass loss during data acquisition. High-resolution lattice fringe images were used to calculate fast Fourier-transformed (FFT) patterns (Chen et al. 2020). The measurement of *d*-spacings was performed using Digital Micrograph software.

Fluid inclusion analysis

Raman micro-spectroscopy was used to determine the composition (both fluid and gas phases) of individual fluid inclusions and to identify different mineral phases at ambient conditions. For this purpose, we employed a HORIBA Jobin Yvon LabRAM HR Evolution confocal micro-Raman system equipped with an Olympus microscope and a frequency-doubled Nd:YAG green laser (532 nm) at Peking University, Beijing, China (Cui et al. 2020). The micro-Raman system is equipped with a 20X long-working distance objective (NA = 0.25), and a stigmatic 800 mm spectrometer with a 1800 groove/mm diffraction grating. The spectrometer was calibrated using a mirror-polished synthetic Si standard. The laser power at the source was 100 mW. The confocal hole was set at 500 μm and the corresponding spectral resolution was ±0.7 cm^{-1}. The laser beam was focused on fluid inclusions close to the upper surface of the thin sections and Raman spectra between 100 and 4000 cm^{-1} were recorded. Data acquisition times for fluid inclusions varied between 30 s and 60 s depending on the morphological and compositional

characteristics of each inclusion and its location. For mineral phases, Raman spectra between 100 and 1300 cm^{-1} were recorded for 10 to 15 seconds and were checked against a common standard database.

Microthermometric measurements were performed at Peking University, Beijing, China, using a LINKAM THMS 600 heating-freezing stage operating in a temperature range of -196 °C to +600 °C. Accuracy of the measurements was ensured by calibration at −56.6 °C and 0 °C using synthetic fluid inclusion standards and pure water. The measurement precision ranged from ±0.1 °C between -120 and -70 °C, to ±0.2 °C between -70 and 100 °C, and ±1 °C between 100 and 600 °C. During each round of measurements, the temperature was first decreased to -120 °C, and then gradually ramped up. The heating rate was reduced to 0.2-0.5 °C min^{-1} close to the phase transitions. Ice-melting temperatures and total homogenization temperatures of the fluid inclusions were measured at a heating rate of 0.5 °C min^{-1}. Melting temperatures of solid CO_2 and clathrate, and homogenization temperatures of CO_2 phases were observed at a heating rate of 0.2-0.5 °C min^{-1}. Salinities of the NaCl–H_2O inclusions were calculated using the final ice-melting temperatures (Bodnar 1993). For tri-phase CO_2-rich inclusions (H_2O-NaCl-CO_2 system), salinities were calculated using the clathrate melting temperatures in combination with liquid-vapor equilibria (Bakker 1997). Program DENSITY and Chueh and Prausnitz's (1967) equation of state were chosen for these

253 calculations.

254

255 ## RESULTS

256 ### Mineral chemistry

257 Fresh granite samples are comprised of abundant K-feldspar ($Ab_{2-6}Or_{94-98}$)
258 and plagioclase ($An_{2-10}Ab_{88-97}Or_{\leq 1}$). Minor albite is also present as exsolution
259 lamellae in K-feldspar. Biotite is a volumetrically significant (up to 10 vol.%)
260 constituent of these rocks, occurring as clusters of platy crystals up to 4 mm
261 across. It contains high FeO and TiO_2 contents (29.8-31.1 and 3.1-3.7 wt.%,
262 respectively) and low MgO levels (3.1-4.0 wt.%, Online Material[1] Table S1).
263 Some biotite crystals contain inclusions of “REE-1” and “REE-2”, which
264 correspond to REE-phosphates with high La_2O_3 and Y_2O_3 contents (4-12 and
265 10-51 wt.%, respectively; Xu et al. 2017). Both these minerals are
266 characterized by low Ce abundances, at or below its detection limit by
267 electron-microprobe analysis. Cerium-poor, Nd-Y-rich bastnäsite-(La) is a
268 fluorocarbonate containing <0.2 wt.% Ce. Its total REE content is high and
269 dominated by La, Nd and Y (up to 30.6, 20.7 and 12.9 wt.% respective oxides,
270 Table 1). To our knowledge, this mineral has not previously been reported in
271 the granites of South China, which generally contain normal bastnäsite-(Ce)
272 and parisite-(Ce) with high Ce but low Y abundances (20-30 wt.% and <4 wt.%
273 respective oxides: Wang et al. 2015; He et al. 2017; Martin et al. 2017). The

composition of cerianite could not be determined with accuracy because of its intimate association with hydrous silicates (Online Material[1] Table S1).

Ce-poor, Nd-Y-rich bastnäsite-(La) structural analysis

The SR-XRD analysis of representative grains of Ce-poor, Nd-Y-rich bastnäsite-(La) demonstrates that it is composed of randomly oriented crystals (Fig. 3). The collected SR-XRD pattern consists of sharp and narrow diffraction peaks, whose full-width-at-half-maximum values indicate particle sizes of <1 μm (Monshi et al. 2012). The measured *d*-spacings (1.137-4.847 Å) are close to, but slightly smaller than, those of Y-poor bastnäsite-(La) (1.149-4.859 Å, Online Material[1] Table S2). This is probably due to the relatively large proportion in the La site of such small cations as Y^{3+} and heavy lanthanides.

Examination of the Ce-poor, Nd-Y-rich bastnäsite-(La) with high-resolution transmission electron microscopy (HRTEM) reveals that its aggregates contain very small crystallites ranging from 5 to 10 nm across (Fig. 4a). The acquired nanoscale compositional maps (including C, O, F, La, Nd and Y) are uniform and show no compositional variation whatsoever (Fig. 4b-g). The boundaries between nanoparticles and larger grains, imaged by HRTEM (Fig. 5 and Online Material[1] Fig. S4), show a gradual transition from crudely aligned nanoparticles to submicrometer-sized grains. The degree of crystallinity within a specific region of the HRTEM foil is directly related to variations between the

295 random and aligned aggregation states of the nanoparticles. Four
296 representative states have been recognized on the basis of the HRTEM
297 images (Fig. 6), described in further detail below.

298 The first type, represented by randomly aggregated nanoparticles, is
299 characterized by randomly oriented lattice fringes and diffraction rings in fast
300 FFT patterns (Fig. 6a). The aggregation state of Ce-poor, Nd-Y-rich
301 bastnäsite-(La) nanoparticles in this case is similar to that of some synthetic
302 examples produced by rapid crystallization: for example, poorly ordered Cu
303 oxalate (Soare et al. 2006) and akaganeite (Nielsen et al. 2014). The second
304 type of aggregate represents a mixture of randomly oriented and crudely
305 aligned nanoparticles (Fig. 6b). They are characterized by FFT patterns
306 featuring both diffraction spots and rings, indicative of ordered and disordered
307 aggregation, respectively. The third type shows parallelism of most lattice
308 fringes and FFT patterns comprising mostly diffraction spots with some fuzzy
309 diffraction rings (Fig. 6c). These features demonstrate that most of the
310 nanoparticles are aligned, although some misoriented lattice fringes indicate
311 that the process of re-arrangement and recrystallization to eliminate the
312 imperfections of the initial aggregation has not finished yet (De Yoreo et al.
313 2015). In the fourth type of aggregate, nanoparticles are assembled into
314 submicrometer-sized crystallites showing well-defined diffraction patterns (Fig.
315 6d). Notably, adjacent crystals are separated from one another by areas

316 composed of disordered nanoparticles, indicating that an oriented aggregation
317 was initiated at multiple sites simultaneously (Banfield et al. 2000). The
318 polycrystalline nature of the Ce-poor, Nd-Y-rich bastnäsite-(La) suggests that
319 the orientation adopted by one crystal is unrelated to those of the adjacent
320 crystals. Atomic plane spacings of about 2.0, 2.9, 3.3, 3.6 and 4.8 Å were
321 observed in lattice fringe images (Fig. 6) and show reasonable agreement with
322 the values measured by SR-XRD (2.0, 2.8, 3.3, 3.5 and 4.8 Å; Online Material[1]
323 Table S2).
324

325 **Fluid inclusions**

326 Two main types of fluid inclusions, CO_2-H_2O-dominated and pure H_2O,
327 were recognized in quartz adjacent to the Ce-poor, Nd-Y-rich bastnäsite-(La)
328 (Fig. 7 and Online Material[1] Fig. S1) using Raman microspectroscopy. The
329 CO_2-H_2O inclusions are pervasive and occur both as primary and secondary
330 inclusions forming a compact three-dimensional network and confined to
331 healed fractures. The gas/liquid filling ratio of these inclusions varies widely
332 (Fig. 7a).

333 Two subtypes were distinguished among them. Subtype IA includes
334 three-phase inclusions (Fig. 7b) with an aqueous fluid, liquid CO_2 (20-60 vol.%
335 of the inclusion), and CO_2 gas (10-25 vol.% of the inclusion). The melting
336 temperature of the CO_2 phase in these inclusions ranges from −57.2 to

337 −58.3 °C. Clathrate melting temperatures range from 3.5 to 8.2 °C,
338 corresponding to salinities of 3.2 to 11.6 wt.% NaCl equivalent (Bakker 1997).
339 These inclusions mostly homogenized to an aqueous phase between 307 and
340 372 °C, and to a gas phase between 349 and 386 °C (Table 2). Subtype IB is
341 represented by CO_2-rich two-phase inclusions composed of an aqueous fluid
342 and a gas bubble, whose volume accounts for 20-70 % of the inclusion. Small
343 daughter crystals of calcite were also observed in some cases (Fig. 7c). The
344 pure H_2O inclusions of Type II are interpreted as secondary in origin (Fig. 7d).
345 The melting temperatures of the ice were measured to range between -4.8 and
346 -7.3 °C, indicating low salinity values from 7.6 to 10.9 wt.% NaCl equivalent
347 (Bodnar 1993). These inclusions homogenize to a liquid phase between 168
348 and 347 °C (Table 2).
349

350 ## DISCUSSION

351 ### Crystallization by particle attachment under REE supersaturation

352 Classical nucleation theory, including terrace-ledge-kink and dislocation
353 growth models, has served as the prevalent conceptual basis for describing
354 crystal nucleation and growth since the 1950s (Burton et al. 1951; Kashchiev
355 2003). However, in the past 30 years, an increasing number of studies have
356 provided convincing evidence for crystallization by particle attachment (CPA)
357 (Penn and Banfield 1999; Zhang et al. 2010; Li et al. 2012; Boneschanscher et

358 al. 2014; De Yoreo et al. 2015). The classical theory works well for the
359 precipitation of low-solubility phases from dilute solutions, but it is not
360 applicable at high degrees of supersaturation (Ivanov et al. 2014).
361 Thermodynamically, the nucleation energy barrier and critical nucleus size
362 should decrease with progressive deviation of the system from equilibrium –
363 for example, due to supersaturation (Ivanov et al. 2014). At low degrees of
364 supersaturation, crystals are expected to grow in accord with the classical
365 nucleation theory because the free-energy barrier is still relatively large
366 (Kashchiev 2003; Wallace et al. 2013). At high levels of supersaturation, the
367 free energy barrier is comparable with thermal energy, and nuclei may be
368 generated in sufficiently large numbers at multiple sites so as to counteract
369 supersaturation (Bray 2002; Scheifele et al. 2013). The particle density will
370 reach a level where a high particle collision rate will facilitate crystal growth by
371 CPA (Cölfen and Antonietti 2008).

372 Multiple intermediate states of atom-to-crystal evolution have been
373 recognized, from simple ions to bulk crystals assembling together by CPA, and
374 involving multi-ionic complexes, oligomers, and nanoparticles (De Yoreo et al.
375 2015). Recent experiments have shown that atoms in nanoscale nuclei
376 (clusters of ordered atoms or ionic groups) may fluctuate reversibly between
377 ordered and disordered states (Jeon et al. 2021). Similarly, fast crystal growth
378 by CPA does not always lead to a well-formed single crystal, but to an

aggregate of slightly misaligned domains (Huang et al. 2004; Soare et al. 2006; Nielsen et al. 2014). Such nanoscale misalignment can be eventually eliminated by reaction with a solution to reduce surface energy (Huang et al. 2004; Nielsen et al. 2014).

We postulate that crystals of Ce-poor, Nd-Y-rich bastnäsite-(La) in the Zhaibei granites developed from initially disordered nanocrystals that assembled into submicrometer-sized particles through CPA (Fig. 6). The examined grains formed aggregates and were not re-arranged to form discrete, structurally uniform single crystals. This indicates that the Ce-poor, Nd-Y-rich bastnäsite-(La) precipitated rapidly from a supersaturated solution, but did not undergo subsequent recrystallization.

REE mineralization under highly oxidized conditions

Supersaturation reported for natural aqueous systems is usually related to microbial activity (Banfield et al. 2000; Penn et al. 2001). However, the temperature of fluids responsible for the REE enrichment in the Zhaibei granites is too high (~170-390 °C) for any microorganism to survive (Brock 1985). Notably, CO_2-rich and aqueous fluid inclusions commonly coexist in these rocks. The gas/liquid volume ratio in such inclusions is variable, but their homogenization temperatures are similar, suggesting CO_2-H_2O immiscibility in their parental fluid (Yardley and Bottrell 1988). The loss of a low-salinity,

400 CO_2-rich phase would increase the pH value of the residual fluid, reduce
401 carbonate activity and increase solute concentrations in the H_2O-dominant
402 fraction (Bowers and Helgeson 1983). Thus, CO_2-H_2O immiscibility should
403 lead to REE supersaturation in the aqueous phase, triggering precipitation of
404 such low-solubility phases as cerianite and REE fluorocarbonates (Xiong 2015;
405 Migdisov et al. 2016). The very different Nd isotopic signature of Ce-poor,
406 Nd-Y-rich bastnäsite-(La) [$\varepsilon Nd_{(t)}$ = 0.9 ± 0.8], in comparison with primary
407 monazite and apatite [$\varepsilon Nd_{(t)}$ = -11.5 ± 0.5] in the parental granite (Xu et al.
408 2017), indicates an external fluid contribution. Although its source has not
409 been ascertained yet owing to the lack of isotopic data for other rock types in
410 the study area, the addition of an externally derived fluid would have certainly
411 resulted in rapid cooling of the hydrothermal system (Carrigan 1986). Thus, we
412 hypothesize that a sudden drop in temperature promoted CO_2-H_2O
413 immiscibility and ultimately triggered the precipitation of Ce-poor, Nd-Y-rich
414 bastnäsite-(La) nanoparticles at multiple nucleation sites. The CPA
415 documented in the present work occurred under moderate-temperature
416 hydrothermal conditions, in contrast to the previously reported cases in
417 synthetic, biogenic and low-temperature geological environments (Banfield et
418 al. 2000; Penn et al. 2001; Hochella et al. 2005), or rapidly quenched melt
419 pockets in Martian meteorites (Zhang et al. 2019).

420 The studied Ce-poor, Nd-Y-rich bastnäsite-(La) is characterized by high

LREE and HREE levels, but extremely low Ce contents. The presence of cerianite and hematitization of ilmenite (Fig. 2f) indicate a high-fO_2 regime. The oxidation of Ce^{3+} to Ce^{4+} is clearly responsible for the observed fractionation between Ce^{4+} and larger and more mobile REE^{3+} cations; e.g., $^{[8]}La^{3+}$ is 18% larger than $^{[8]}Ce^{4+}$ (Shannon 1976). Owing to the low solubility of CeO_2 in fluids (Xiong 2015), cerianite was precipitated as veinlets associated with the hydrous Al-Fe-rich silicate mineral (Fig. 2e). The logfO_2 values of Jurassic to Early Cretaceous granites in South China range from -0.83 to +4.22 relative to the Ni-NiO buffer (Li et al. 2017), which is too low for Ce oxidation (Burnham and Berry 2014). The possible sources of oxidizing components could be the incursion of external fluids into the granites at the subsolidus stage, derived either from dehydrated lithospheric material, which subducted beneath the amalgamated China continent in the early Jurassic (Liu et al. 2017), or from meteoric sources. The fO_2 levels in arc magmas are estimated to have been insufficient for Ce oxidation (Kelley and Cottrell 2012; Burnham and Berry 2014). Incursion of meteoric water into the subsolidus granites could result in high $f(O_2)$ values and oxidation of Ce^{3+} to Ce^{4+} while not affecting the rest of the REE budget. This process could have also triggered a rapid temperature drop and the precipitation of nanocrystalline HREE-rich carbonates with a strong Ce depletion.

The poly-crystalline Ce-poor, HREE-rich minerals with a poorly-ordered

structure and numerous defects and dislocations readily decompose during weathering (Wilson 2004), resulting in REE removal from the precursor granite. Aqueous complexes can readily fractionate HREE from LREE during intense weathering. In particular, HREE form stronger complexes with carbonate and fluoride ligands than LREE at ambient temperature (Wood 1990; Haas et al. 1995; Tropper et al. 2011, 2013; Mair et al. 2017), thereby increasing the concentration of the former in the fluid and promoting their transport and adsorption onto clay minerals. This mechanism may explain the anomalous HREE enrichment of some South China IAD.

IMPLICATIONS

The detailed HRTEM study of Ce-poor, Nd-Y-rich bastnäsite-(La) presented above documented several successive steps in the aggregation of nanoparticles to form submicrometer-sized crystallites. The observed morphological evolution is best explained by CPA under supersaturated conditions, as there is no HRTEM evidence for crystal-growth by terrace or dislocation-constrained mechanisms. Cerium oxidation and its decoupling from trivalent REE, which produced Ce-poor, HREE-rich minerals, and hematitization of ilmenite attest to the high fO_2 values in the fluid. We infer that the interaction of the hydrothermal system with external meteoric fluids led to a sudden drop in temperature and CO_2-H_2O immiscibility, which triggered REE

463 supersaturation and the deposition of nanocrystalline Ce-poor, Nd-Y-rich
464 bastnäsite-(La) and cerianite in the Zhaibei granites. This process has
465 far-reaching implications for the understanding of the precursors and
466 prerequisite conditions involved in the development of HREE-rich IAD.
467 Nano-mineralization of the type described in the present contribution could be
468 a “missing link” between magmatic REE hosts, which have low solubility in
469 fluids, and ion-exchangeable phases in the weathering profile. The
470 polycrystalline nano-aggregates of REE minerals are clearly more susceptible
471 to weathering than primary monazite, zircon, or apatite (Fu et al. 2019). A
472 detailed mineralogical study of precursor igneous rocks is thus essential for
473 constraining the HREE exploration potential of IAD and for developing a
474 comprehensive REE metallogenic model for these deposits.

475

476 **ACKNOWLEDGEMENTS AND FUNDING**

477 We thank Bin Wu and Zhenyu Chen for mineral analyses. Zheng Zhao,
478 Yan Li, Ming Tang and Jin Liu are gratefully acknowledged for their assistance
479 in the field and data discussions. We are grateful to Daniel E. Harlov for
480 handling this manuscript and two anonymous reviewers for their constructive
481 comments. This research was supported financially by the National Natural
482 Science Foundation of China (41825008) and Guangxi Natural Science
483 Foundation (2020GXNSFGA297003). MS acknowledges support from the

484 UK-RI Natural Environment Research Council grant NE/V008935/1. J.K. was
485 supported by the Czech Science Foundation GACR EXPRO (grant number
486 19-29124X).

487

488 **REFERENCES CITED**

489 Bakker, R.J. (1997) Clathrates: Computer programs to calculate fluid inclusion
490 VX properties using clathrate melting temperatures. Computers &
491 Geosciences, 23, 1-18.

492 Balaram, V. (2019) Rare earth elements: A review of applications, occurrence,
493 exploration, analysis, recycling, and environmental impact. Geoscience
494 Frontiers, 10, 1285-1303.

495 Banfield, J.F., Welch, S.A., Zhang, H.Z., Ebert, T.T., and Penn, R.L. (2000)
496 Aggregation-based crystal growth and microstructure development in
497 natural iron oxyhydroxide biomineralization products. Science, 289,
498 751-754.

499 Bao, Z., and Zhao, Z. (2008) Geochemistry of mineralization with
500 exchangeable REY in the weathering crusts of granitic rocks in South
501 China. Ore Geology Reviews, 33, 519-535.

502 Bernhardt, D., and Reilly, I.I.J.F. (2020) Mineral Commodity Summaries 2020.
503 US Geological Survey.

504 Bodnar, R. (1993) Revised equation and table for determining the freezing

point depression of H_2O-NaCl solutions. Geochimica et Cosmochimica Acta, 57, 683-684.

Boneschanscher, M.P., Evers, W.H., Geuchies, J.J., Altantzis, T., Goris, B., Rabouw, F.T., van Rossum, S.A.P., van der Zant, H.S.J., Siebbeles, L.D.A., Van Tendeloo, G., Swart, I., Hilhorst, J., Petukhov, A.V., Bals, S., and Vanmaekelbergh, D. (2014) Long-range orientation and atomic attachment of nanocrystals in 2D honeycomb superlattices. Science, 344, 1377-1380.

Borst, A.M., Smith, M.P., Finch, A.A., Estrade, G., Villanova-de-Benavent, C., Nason, P., Marquis, E., Horsburgh, N.J., Goodenough, K.M., Xu, C., Kynicky, J., and Geraki, K. (2020) Adsorption of rare earth elements in regolith-hosted clay deposits. Nature Communications, 11, 4386.

Bowers, T.S., and Helgeson, H.C. (1983) Calculation of thermodynamic and geochemical consequences of non-ideal mixing in the system H_2O-CO_2-NaCl on phase relations in geologic systems: equation of state for H_2O-CO_2-NaCl fluids at high pressures and temperatures. Geochimica et Cosmochimica Acta, 47, 1247-1275.

Bray, A.J. (2002) Theory of phase-ordering kinetics. Advances in Physics, 51, 481-587.

Brock, T.D. (1985) Life at high temperatures. Science, 230, 132-138.

Burnham, A.D., and Berry, A.J. (2014) The effect of oxygen fugacity, melt

composition, temperature and pressure on the oxidation state of cerium in silicate melts. Chemical Geology, 366, 52-60.

Burton, W.K., Cabrera, N., and Frank, F.C. (1951) The growth of crystals and the equilibrium structure of their surfaces. Philosophical Transactions of the Royal Society of London. Series A, Mathematical and Physical Sciences, 243, 299-358.

Carrigan, C.R. (1986) A two-phase hydrothermal cooling model for shallow intrusions. Journal of volcanology and geothermal research, 28, 175-192.

Chakhmouradian, A.R., Reguir, E.P., Zaitsev, A.N., Couëslan, C., Xu, C., Kynicky, J., Mumin, A.H., and Yang, P. (2017) Apatite in carbonatitic rocks: Compositional variation, zoning, element partitioning and petrogenetic significance. Lithos, 274-275, 188-213.

Chen, S., Zhang, Y., Zhang, X., Zhao, J., Zhao, Z., Su, X., Hua, Z., Zhang, J., Cao, J., Feng, J., Wang, X., Li, X., Qi, J., Li, J., and Gao, P. (2020) General decomposition pathway of organic–inorganic hybrid perovskites through an intermediate superstructure and its suppression mechanism. Advanced Materials, 32, 2001107.

Chueh, P.L., and Prausnitz, J.M. (1967) Vapor-liquid equilibria at high pressures. Vapor-phase fugacity coefficients in nonpolar and quantum-gas mixtures. Industrial & Engineering Chemistry Fundamentals, 6, 492-498.

547 Cölfen, H., and Antonietti, M. (2008) Mesocrystals and nonclassical
548 crystallization. Ch. 9 (Wiley).
549 Cui, H., Zhong, R., Xie, Y., Yuan, X., Liu, W., Brugger, J., and Yu, C. (2020)
550 Forming sulfate-and REE-rich fluids in the presence of quartz. Geology,
551 48, 145-148.
552 De Yoreo, J.J., Gilbert, P.U.P.A., Sommerdijk, N.A.J.M., Penn, R.L., Whitelam,
553 S., Joester, D., Zhang, H.Z., Rimer, J.D., Navrotsky, A., Banfield, J.F.,
554 Wallace, A.F., Michel, F.M., Meldrum, F.C., Cölfen, H., and Dove, P.M.
555 (2015) Crystallization by particle attachment in synthetic, biogenic, and
556 geologic environments. Science, 349, aaa6760.
557 Estrade, G., Marquis, E., Smith, M., Goodenough, K., and Nason, P. (2019)
558 REE concentration processes in ion adsorption deposits: evidence from
559 the Ambohimirahavavy alkaline complex in Madagascar. Ore Geology
560 Reviews, 112, 103027.
561 Fu, W., Li, X., Feng, Y., Feng, M., Peng, Z., Yu, H., and Lin, H. (2019) Chemical
562 weathering of S-type granite and formation of Rare Earth Element
563 (REE)-rich regolith in South China: Critical control of lithology. Chemical
564 Geology, 520, 33-51.
565 Gulley, A.L., Nassar, N.T., and Xun, S. (2018) China, the United States, and
566 competition for resources that enable emerging technologies.
567 Proceedings of The National Academy of Sciences ,115, 4111-4115.

568 Haas, J.R., Shock, E.L., and Sassani, D.C. (1995) Rare earth elements in
569 hydrothermal systems: estimates of standard partial molal thermodynamic
570 properties of aqueous complexes of the rare earth elements at high
571 pressures and temperatures. Geochimica et Cosmochimica Acta, 59,
572 4329-4350.
573 Hammersley, A.P. (1997) FIT2D: An Introduction and Overview: European
574 Synchrotron Radiation Facility Internal Report ESRF97HA02T, 68, 58.
575 Harlov, D.E. (2015) Apatite: a fingerprint for metasomatic processes. Elements,
576 11, 171-176.
577 Harlov, D.E., and Förs er, H.J. (2003) Fluid-induced nucleation of (Y+
578 REE)-phosphate minerals within apatite: Nature and experiment. Part II.
579 Fluorapatite. American Mineralogist, 88, 1209-1229.
580 He, C., Xu, C., Zhao, Z., Kynicky, J., Song, W.L., and Wang, L.Z. (2017)
581 Petrogenesis and mineralization of REE-rich granites in Qingxi and
582 Guanxi, Nanling region, South China. Ore Geology Reviews, 81, 309-325.
583 Hochella Jr, M.F., Kasama, T., Putnis, A., Putnis, C.V., and Moore, J.N. (2005)
584 Environmentally important, poorly crystalline Fe/Mn hydrous oxides:
585 ferrihydrite and a possibly new vernadite-like mineral from the Clark Fork
586 River Superfund Complex. American Mineralogist, 90, 718-724.
587 Huang, F., Gilbert, B., Zhang, H.H., and Banfield, J.F. (2004) Reversible,
588 surface-controlled structure transformation in nanoparticles induced by an

aggregation state. Physical Review Letters, 92, 155501.

Ivanov, V.K., Fedorov, P.P., Baranchikov, A.Y., and Osiko, V.V. (2014) Oriented attachment of particles: 100 years of investigations of non-classical crystal growth. Russian Chemical Reviews, 83, 1204-1222.

Janots, E., Bernier, F., Brunet, F., Munoz, M., Trcera, N., Berger, A., and Lanson, M. (2015) Ce (III) and Ce (IV)(re) distribution and fractionation in a laterite profile from Madagascar: insights from in situ XANES spectroscopy at the Ce LIII-edge. Geochimica et Cosmochimica Acta, 153, 134-148.

Jeon, S., Heo, T., Hwang, S.Y., Ciston, J., Bustillo, K.C., Reed, B.W., Ham, J.M., Kang, S.S., Kim, S.G., Lim, J., Lim, K., Kim, J.S., Kang, M.H., Bloom, R.S., Hong, S., Kim, K., Zettl, A., Kim, W.Y., Ercius, P., Park, J., and Lee, W.C. (2021) Reversible disorder-order transitions in atomic crystal nucleation. Science, 371, 498-503.

Kalvig, P., and Machacek, E. (2018) Examining the rare-earth elements (REE) supply-demand balance for future global wind power scenarios. GEUS Bulletin, 41, 87-90.

Kashchiev, D. (2003) Thermodynamically consistent description of the work to form a nucleus of any size. The Journal of Chemical Physics, 118, 1837-1851.

Kelley, K.A., and Cottrell, E. (2012) The influence of magmatic differentiation

on the oxidation state of Fe in a basaltic arc magma. Earth and Planetary Science Letters, 329, 109-121.

Li, D.S., Nielsen, M.H., Lee, J.R.I., Frandsen, C., Banfield, J.F., and De Yoreo, J.J. (2012) Direction-specific interactions control crystal growth by oriented attachment. Science, 336, 1014-1018.

Li, X.H., Chen, Z.G., Li, D.Y., and Li, W.X. (2003) Jurassic gabbro-granite-syenite suites from southern Jiangxi Province, SE China: age, origin, and tectonic significance. International Geology Review, 45, 898-921.

Li, X.Y., Chi, G.X., Zhou, Y.Z., Deng, T., and Zhang, J.R. (2017) Oxygen fugacity of Yanshanian granites in South China and implications for metallogeny. Ore Geology Reviews, 88, 690-701.

Li, Z.X., and Li, X.H. (2007) Formation of the 1300-km-wide intracontinental orogen and postorogenic magmatic province in Mesozoic South China: a flat-slab subduction model. Geology, 35, 179-182.

Liu, S.F., Gurnis, M., Ma, P.F., and Zhang, B. (2017) Reconstruction of northeast Asian deformation integrated with western Pacific plate subduction since 200 Ma. Earth-Science Reviews, 175, 114-142.

Mair, P., Tropper, P., Harlov, D.E., and Manning, C.E. (2017) The solubility of $CePO_4$ monazite and YPO_4 xenotime in KCl-H_2O fluids at 800 °C and 1.0 GPa: Implications for REE transport in high-grade crustal fluids. American

631 Mineralogist: Journal of Earth and Planetary Materials, 102, 2457-2466.
632 Mao, J.W., Xie, G.Q., Guo, C.L., Yuan, S.D., Cheng, Y.B., and Chen, Y.C.
633 (2008) Spatial temporal distribution of Mesozoic ore deposits in South
634 China and their metallogenic settings. Geological Journal of China
635 Universities, 14, 510–526.
636 Martin L.Y.H., and Zhou, M.F. (2020) The role of clay minerals in formation of
637 the regolith-hosted heavy rare earth element deposits. American
638 Mineralogist, 105, 92-108.
639 Martin L.Y.H., Zhao, W.W., and Zhou, M.F. (2017) Nature of parent rocks,
640 mineralization styles and ore genesis of regolith-hosted REE deposits in
641 South China: an integrated genetic model. Journal of Asian Earth
642 Sciences, 148, 65-95.
643 Migdisov A., Williams-Jones, A.E., Brugger, J., and Caporuscio, F.A. (2016)
644 Hydrothermal transport, deposition, and fractionation of the REE:
645 Experimental data and thermodynamic calculations. Chemical Geology,
646 439, 13-42.
647 Monshi, A., Foroughi, M.R., and Monshi, M.R. (2012) Modified Scherrer
648 equation to estimate more accurately nano-crystallite size using XRD.
649 World Journal of Nano Science and Engineering, 2, 154-160.
650 Nielsen, M.H., Li, D.S., Zhang, H.Z., Aloni, S., Han, T.Y.J., Frandsen, C., Seto,
651 J., Banfield, J.F., Cölfen, H., and De Yoreo, J.J. (2014) Investigating

processes of nanocrystal formation and transformation via liquid cell TEM. Microscopy and Microanalysis, 20, 425-436.

Penn, R.L., and Banfield, J.F. (1999) Morphology development and crystal growth in nanocrystalline aggregates under hydrothermal conditions: insights from titania. Geochimica et Cosmochimica Acta, 63, 1549-1557.

Penn, R.L., Zhu, C., Xu, H., and Veblen, D.R. (2001) Iron oxide coatings on sand grains from the Atlantic coastal plain: high-resolution transmission electron microscopy characterization. Geology, 29, 843-846.

Prameswara, G., Trisnawati, I., Mulyono, P., Prasetya, A., and Petrus, H.T.B.M. (2021) Leaching behaviour and kinetic of light and heavy rare earth elements (REE) from zircon tailings in Indonesia. The Journal of the Minerals, Metals & Materials Society, 73, 988-998.

Rice, S.B., Koo, J.Y., Disko, M.M., and Treacy, M.M.J. (1990) On the imaging of Pt atoms in zeolite frameworks. Ultramicroscopy, 34, 108-118.

Sanematsu, K., Kon, Y., Imai, A., Watanabe, K., and Watanabe, Y. (2013) Geochemical and mineralogical characteristics of ion-adsorption type REE mineralization in Phuket, Thailand. Mineralium Deposita, 48, 437-451.

Scheifele, B., Saika-Voivod, I., Bowles, R.K., and Poole, P.H. (2013) Heterogeneous nucleation in the low-barrier regime. Physical Review E, 87, 042407.

673 Shannon, R.D. (1976) Revised effective ionic radii and systematic studies of
674 interatomie distances in halides and chaleogenides. Acta
675 Crystallographica Section A: Crystal Physics, Diffraction, Theoretical and
676 General Crystallography, 32, 751-767.
677 Soare, L.C., Bowen, P., Lemaitre, J., and Hofmann, H. (2006) Precipitation of
678 nanostructured copper oxalate: substructure and growth mechanism. The
679 Journal of Physical Chemistry B, 110, 17763-17771.
680 Sun, F., Xu, X., Zou, H., and Xia, Y. (2015) Petrogenesis and magmatic
681 evolution of ~130 Ma A-type granites in Southeast China. Journal of Asian
682 Earth Sciences, 98, 209-224.
683 Tropper, P., Manning, C.E., and Harlov, D.E. (2011) Solubility of $CePO_4$
684 monazite and YPO_4 xenotime in H_2O and H_2O-NaCl at 800 °C and 1 GPa:
685 Implications for REE and Y transport during high-grade metamorphism.
686 Chemical Geology, 282, 58-66.
687 Tropper, P., Manning, C.E., and Harlov, D.E. (2013) Experimental
688 determination of $CePO_4$ and YPO_4 solubilities in H_2O-NaF at 800 °C and 1
689 GPa: Implications for rare earth element transport in high‐grade
690 metamorphic fluids. Geofluids, 13, 372-380.
691 Wallace, A.F., Hedges, L.O., Fernandez-Martinez, A., Raiteri, P., Gale, J.D.,
692 Waychunas, G.A., Whitelam, S., Banfield, J.F., and De Yoreo, J.J. (2013)
693 Microscopic evidence for liquid-liquid separation in supersaturated $CaCO_3$

694 solutions. Science, 341, 885-889.

695 Wang, L.Z., Xu, C., Zhao, Z., Song, W.L., and Kynicky, J. (2015) Petrological
696 and geochemical characteristics of Zhaibei granites in Nanling region,
697 Southeast China: implications for REE mineralization. Ore Geology
698 Reviews, 64, 569-582.

699 Wang, R.C., Xie, L., Lu, J.J., Zhu, J.C., and Chen, J. (2017) Diversity of
700 Mesozoic tin-bearing granites in the Nanling and adjacent regions, South
701 China: distinctive mineralogical patterns. Science China Earth Sciences,
702 60, 1909-1919.

703 Wang, Y., Fan, W., Zhang, G., and Zhang, Y. (2013) Phanerozoic tectonics of
704 the South China Block: key observations and controversies. Gondwana
705 Research, 23, 1273-1305.

706 Wilson, M.J. (2004) Weathering of the primary rock-forming minerals:
707 processes, products and rates. Clay Minerals, 39, 233-266.

708 Wood, S.A. (1990) The aqueous geochemistry of the rare-earth elements and
709 yttrium: 1. Review of available low temperature data for inorganic
710 complexes and the inorganic REE speciation of natural waters. Chemical
711 Geology, 82, 159-186.

712 Xiong, Y.L. (2015) Experimental Determination of Solubility of Cerianite (CeO_2)
713 in High Ionic Srength Solutions at Elevated Temperatures. An Analog to
714 Tetravalent Actinides (No. SAND2015-9186C). Sandia National

715 Lab.(SNL-NM), Albuquerque, NM (United States).

716 Xu, C., Kynický, J., Smith, M.P., Kopriva, A., Brtnický, M., Urubek, T., Yang,
717 Y.H., Zhao, Z., He, C., and Song, W.L. (2017) Origin of heavy rare earth
718 mineralization in South China. Nature Communications, 8, 14598.

719 Yardley, B., and Bottrell, S. (1988) Immiscible fluids in metamorphism:
720 implications of two-phase flow for reaction history. Geology, 16, 199-202.

721 Zhang, A.C., Wang, S.Z., Tomioka, N., Lu, X.C., Ding, Z.Y., Ma, C., Wang, P.,
722 Chen, J.N., Xu, S., Gu, L.X., Bai, Y.Q., Li, Y., Sakamoto, N., and Wang,
723 R.C. (2019) An example of high-T, high-symmetry crystallization: spherical
724 (Mg, Fe)-oxides formed by particle attachment in the shocked Martian
725 meteorite Northwest Africa 7755. American Mineralogist, 104, 150-157.

726 Zhang, J., Huang, F., and Lin, Z. (2010) Progress of nanocrystalline growth
727 kinetics based on oriented attachment. Nanoscale, 2, 18-34.

728 Zhou, B.X., Sun, T., Shen, W., Shu, L., and Niu, Y. (2006) Petrogenesis of
729 Mesozoic granitoids and volcanic rocks in South China: a response to
730 tectonic evolution. Episodes, 29, 26-33.

731 Zhou, Y., Liang, X., Wu, S., Cai, Y., Liang, X., Shao, T., Wang, C., Fu, J., and
732 Jiang, Y. (2015) Isotopic geochemistry, zircon U–Pb ages and Hf isotopes
733 of A-type granites from the Xitian W–Sn deposit, SE China: Constraints on
734 petrogenesis and tectonic significance. Journal of Asian Earth Sciences,
735 105, 122-139.

736

737 **Endnote:**

738 [1]Deposit item ##, Online Materials. Deposit items are free to all readers and
739 found on the MSA website, via the specific issue's Table of Contents (go to
740 http://www.minsocam.org/MSA/AmMin/##).

741

742 **FIGURE CAPTIONS**

743 **FIGURE 1.** Distribution of granites in southeastern China and the location of
744 the Zhaibei granite (modified after Wang et al. 2017).

745

746 **FIGURE 2.** Representative photomicrographs of minerals from the Zhaibei
747 granites. (a) As-yet unidentified phases "REE-1" and "REE-2" formed by
748 alteration of magmatic fluorapatite (Ap). (b) Ce-poor, Nd-Y-rich bastnäsite-(La)
749 [Bast (La)] in fractures cross-cutting K-feldspar (Kfs) and plagioclase (Pl). (c)
750 Encrustations of Ce-poor, Nd-Y-rich bastnäsite-(La) lining a cavity interstitial to
751 quartz (Q). (d) Hydrous Al-Fe-rich silicate at the contact between Ce-poor and
752 Nd-Y-rich bastnäsite-(La), biotite (Bt), and K-feldspar. (e) Veinlet of cerianite
753 intergrown with an unidentified hydrous Al-Fe-rich silicate. (f) Ilmenite (Ilm)
754 partially converted to hematite (Hem).

755

756 **FIGURE 3.** In-situ synchrotron radiation-induced X-ray diffraction analysis of

Ce-poor, Nd-Y-rich bastnäsite-(La) [Bast (La)]. (a) Location of the analyzed area within a 75-μm circle. (b) X-ray diffraction pattern and diffraction rings.

FIGURE 4. High-angle annular dark-field scanning transmission electron microscopy (HAADF STEM) image showing nanoparticles of Ce-poor, Nd-Y-rich bastnäsite-(La) (a) and nano-scale compositional maps (b-g) showing a uniform distribution of C, O, F, La, Nd and Y within the nanoparticles.

FIGURE 5. HRTEM image of an irregular boundary between submicrometer-sized particles and nanoparticles of Ce-poor, Nd-Y-rich bastnäsite-(La).

FIGURE 6. HRTEM images of Ce-poor, Nd-Y-rich bastnäsite-(La). (a) Nanoparticles of randomly aggregated Ce-poor, Nd-Y-rich bastnäsite-(La). Their FFT pattern shows diffraction rings. (b) Nanoparticles partially aggregated by oriented attachment with FFT pattern exhibiting diffraction spots and rings. (c) Advanced stage of nanoparticle assembly with some local misalignment in particle orientation (red circles). Note regular diffraction spots in the FFT pattern. (d) Aggregated nanoparticles showing a near-perfect alignment and a well-defined diffraction pattern.

778

779 **FIGURE 7.** Representative photomicrographs of fluid inclusions in quartz. (a)
780 CO_2-H_2O inclusions (Type I) with various gas/liquid filling ratios. (b)
781 Three-phase CO_2-H_2O type inclusions. (c) Calcite daughter crystal (Cal) in a
782 fluid inclusion. (d) CO_2-rich inclusions coexisting with aqueous (Type II) fluid
783 inclusions.

784

785

786

787

788

789

790

This is the peer-reviewed, final accepted version for American Mineralogist, published by the Mineralogical Society of America.
The published version is subject to change. Cite as Authors (Year) Title. American Mineralogist, in press.
DOI: https://doi.org/10.2138/am-2022-8309. http://www.minsocam.org/

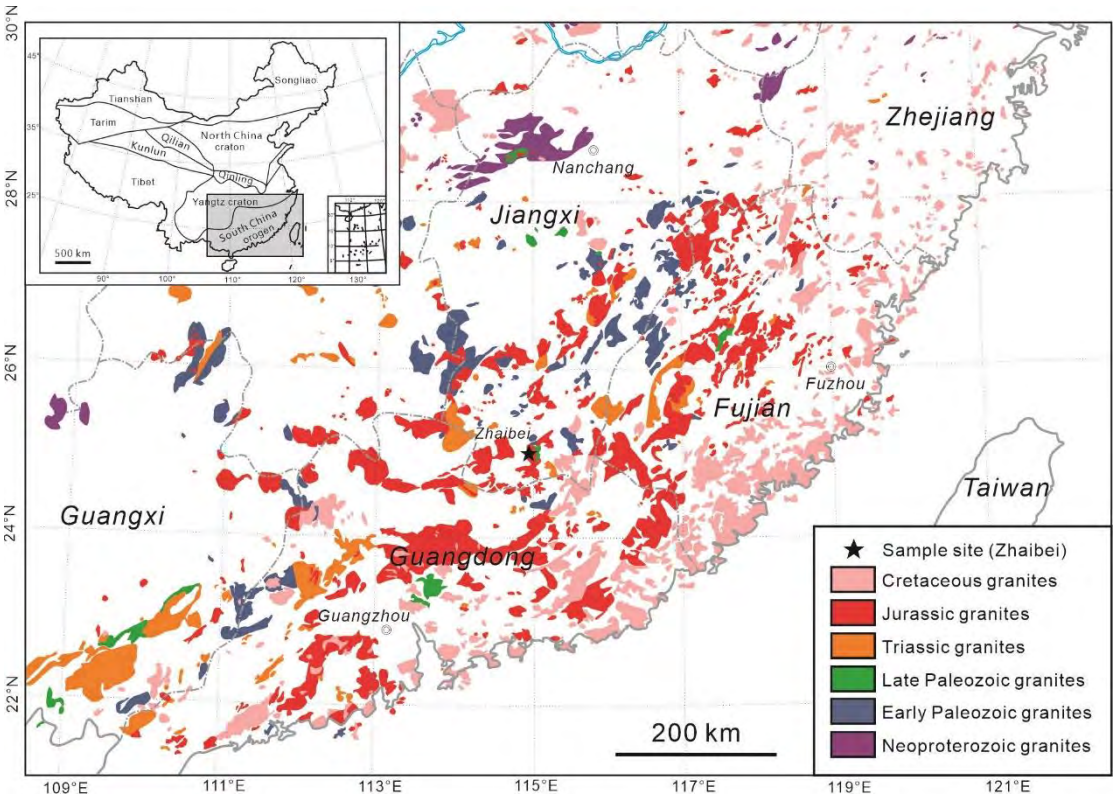

FIGURE 1

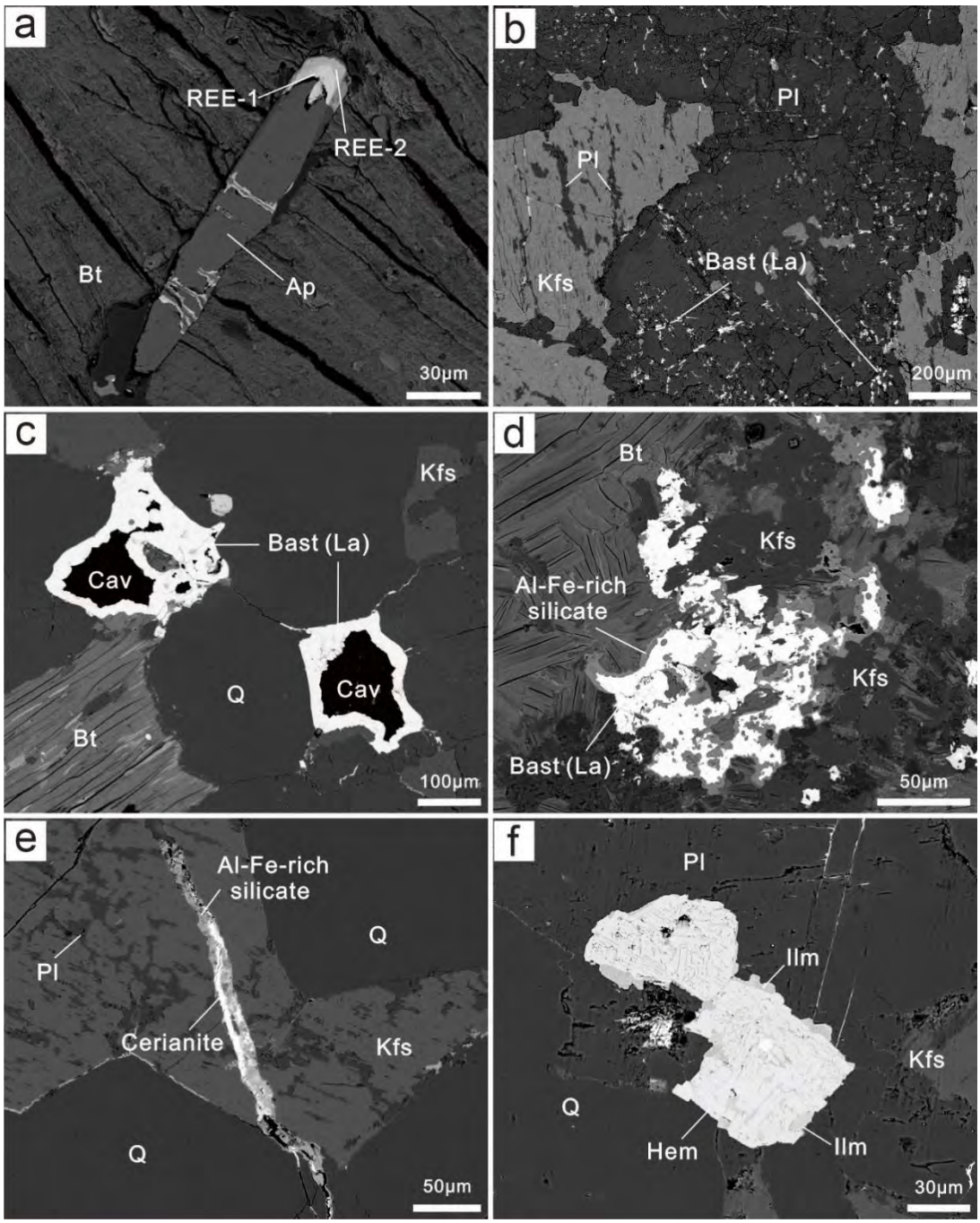

794

795 **FIGURE 2**

796

This is the peer-reviewed, final accepted version for American Mineralogist, published by the Mineralogical Society of America.
The published version is subject to change. Cite as Authors (Year) Title. American Mineralogist, in press.
DOI: https://doi.org/10.2138/am-2022-8309. http://www.minsocam.org/

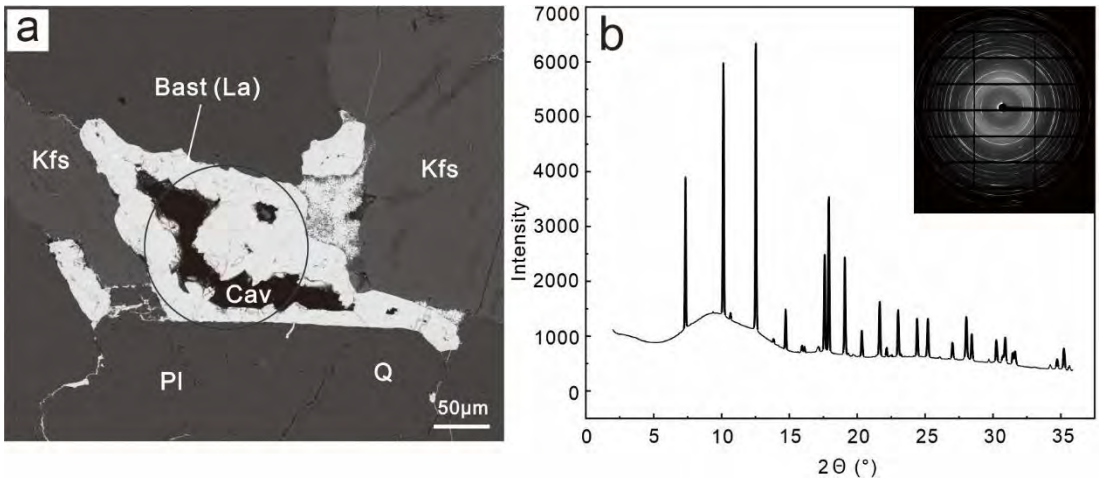

FIGURE 3

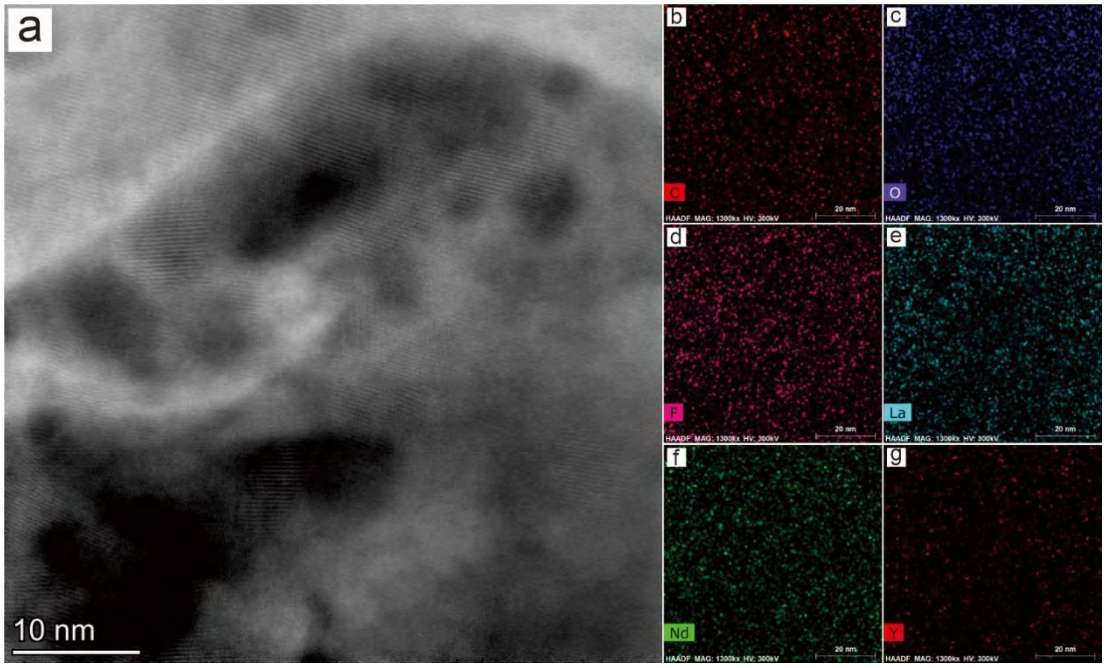

FIGURE 4

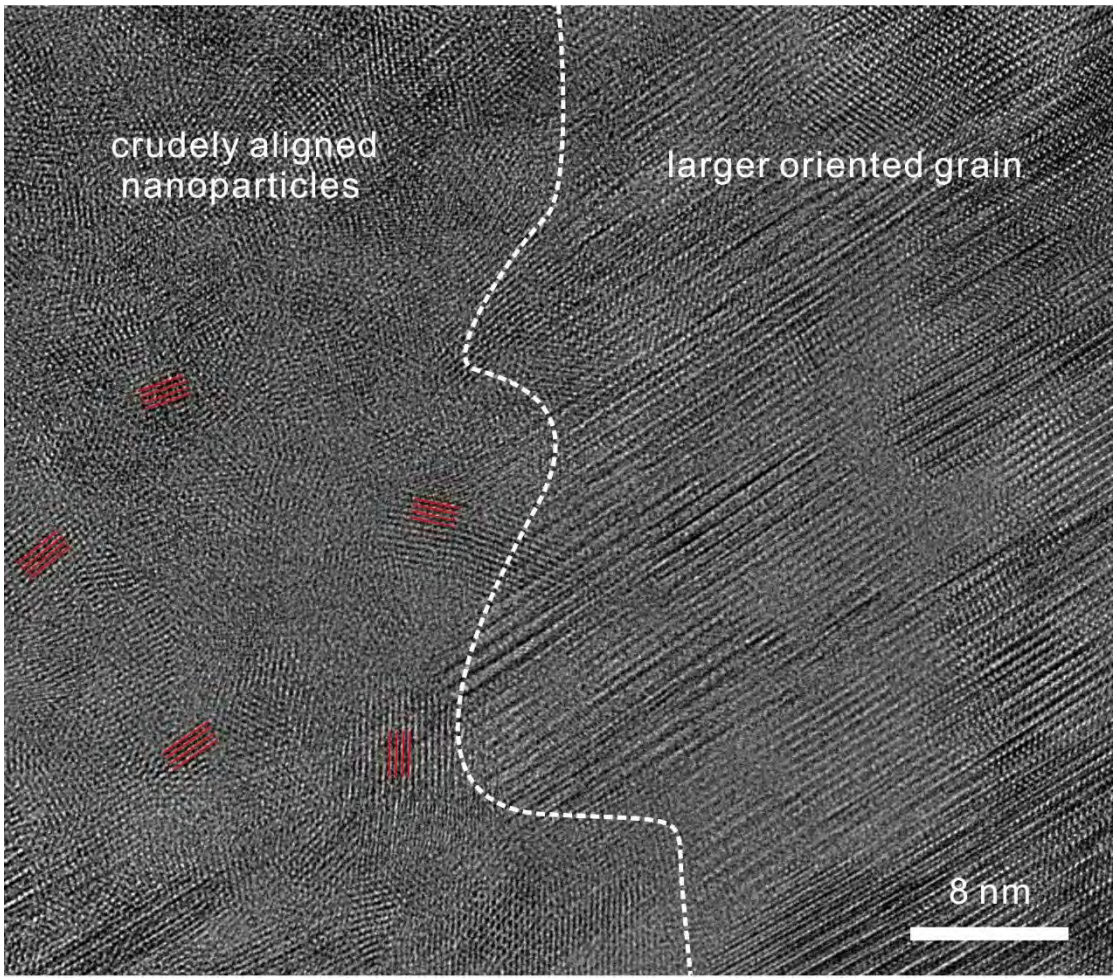

806

807 **FIGURE 5**

808

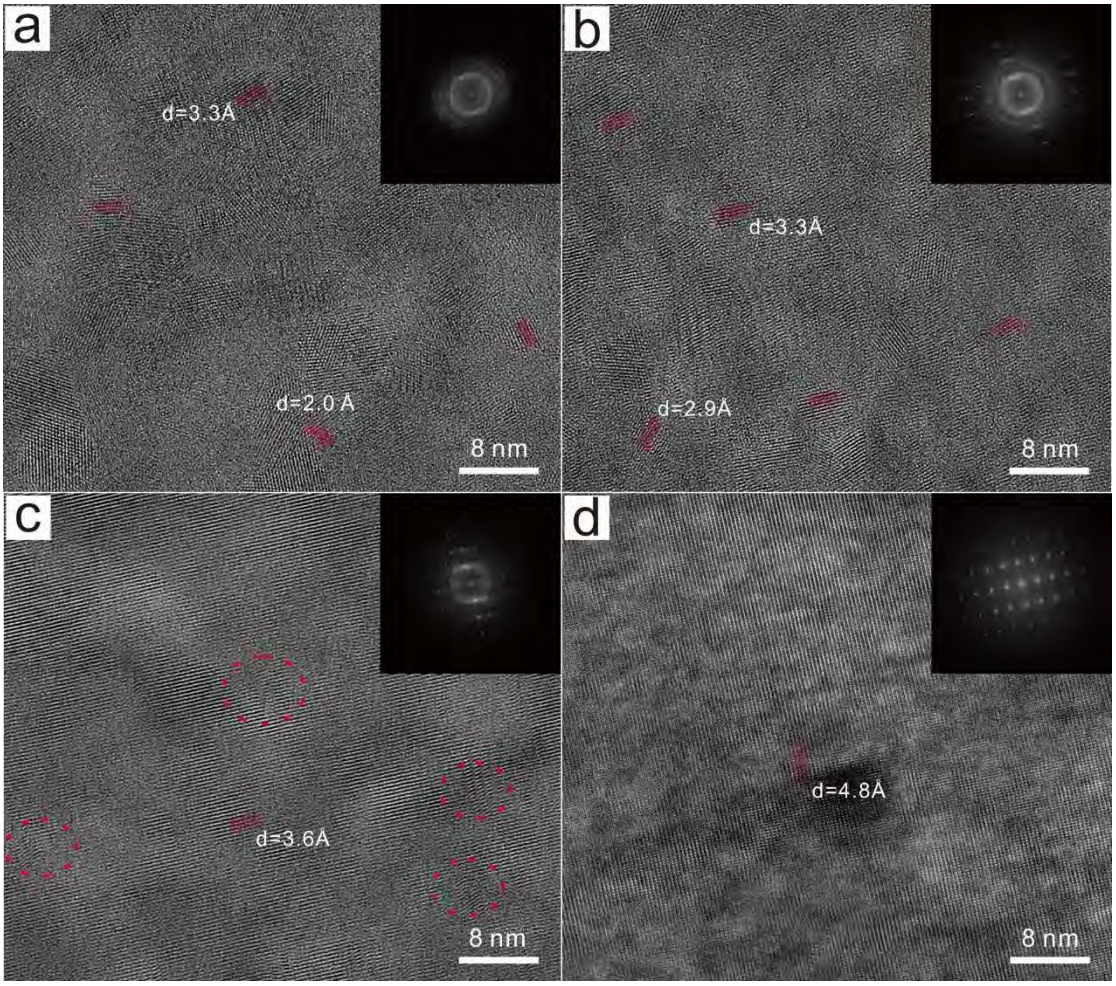

FIGURE 6

This is the peer-reviewed, final accepted version for American Mineralogist, published by the Mineralogical Society of America.
The published version is subject to change. Cite as Authors (Year) Title. American Mineralogist, in press.
DOI: https://doi.org/10.2138/am-2022-8309. http://www.minsocam.org/

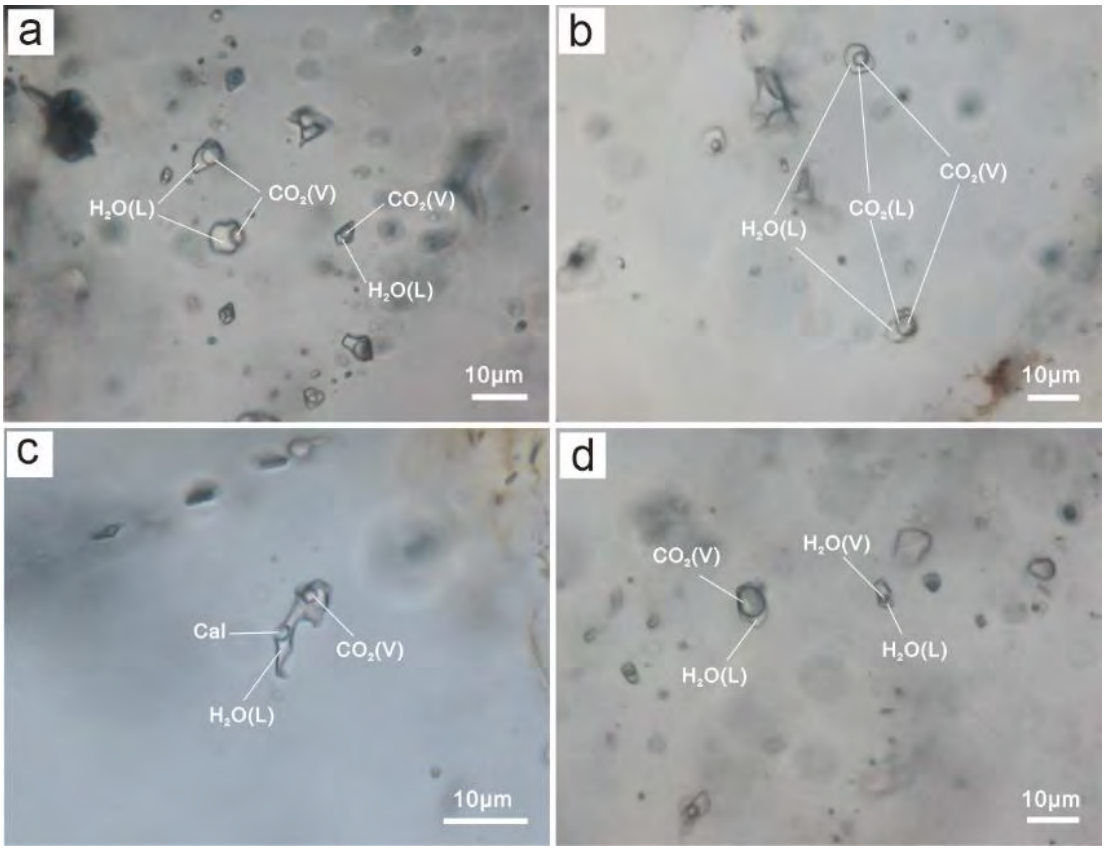

FIGURE 7

824 Table 1. Compositions (wt.%) of Ce-poor, Nd-Y-rich bastnäsite-(La) in the Zhaibei granites

Sample	1	2	3	4	5	6	7	8	9	10
P_2O_5	0.28	0.37	0.25	0.28	0.23	0.17	0.41	0.12	0.46	0.11
SiO_2	0.02	0.03	0.06	0.04	0.02	0.05	0.13	0.08	bdl	0.01
ThO_2	bdl	0.01	bdl	bdl	bdl	bdl	0.07	0.03	bdl	bdl
Al_2O_3	bdl	0.06	bdl	bdl	bdl	0.01	0.09	bdl	0.02	0.03
Y_2O_3	9.98	6.03	9.36	9.75	11.36	9.88	7.58	10.72	9.36	9.61
La_2O_3	29.62	29.67	29.45	29.44	30.01	29.29	29.51	29.68	30.06	29.71
Ce_2O_3	0.11	bdl	0.15	0.01	0.24	bdl	bdl	0.24	0.15	0.05
Pr_2O_3	5.11	6.24	5.24	5.29	4.71	5.07	5.13	5.11	4.83	5.15
Nd_2O_3	17.74	20.68	17.97	18.15	17.00	18.27	19.14	17.35	18.08	18.04
Sm_2O_3	3.75	4.25	3.88	3.80	3.76	3.99	4.01	3.97	4.03	4.06
Eu_2O_3	0.36	0.56	0.52	bdl	0.40	0.63	0.51	0.25	0.11	0.23
Gd_2O_3	2.97	2.46	3.06	2.84	3.41	3.08	2.74	3.10	3.13	3.10
Dy_2O_3	2.05	1.81	1.84	1.96	2.24	1.97	1.88	2.25	2.01	2.06
Ho_2O_3	1.48	1.57	1.26	1.09	1.24	1.12	1.48	1.41	1.55	1.57
Er_2O_3	0.11	0.26	bdl	0.06	0.27	bdl	0.27	0.16	0.37	0.32
Tm_2O_3	bdl	bdl	0.07	0.18	0.05	bdl	bdl	0.02	bdl	bdl
Yb_2O_3	0.54	0.44	0.39	bdl	0.02	0.19	0.23	0.23	0.19	0.30
CaO	0.52	0.52	0.54	0.53	0.48	0.55	0.51	0.66	0.47	0.54
FeO	bdl	0.02	0.05	0.08	0.10	0.05	bdl	0.01	bdl	0.01
K_2O	bdl	0.02	0.01	0.01	0.01	0.05	0.01	0.03	bdl	0.01
F	5.66	5.56	5.24	6.04	5.13	5.68	8.02	4.98	4.77	5.52
CO_2	21.27	20.94	21.12	21.04	21.72	21.31	20.81	21.71	21.22	21.32
H_2O	1.67	1.65	1.83	1.44	2.01	1.65	0.47	2.06	2.09	1.73
O=F	-2.38	-2.34	-2.21	-2.54	-2.16	-2.39	-3.38	-2.10	-2.01	-2.32
Total	100.86	100.81	100.08	99.49	102.25	100.62	99.62	102.07	100.89	101.16
Formulae based on 1 cation										
P	0.008	0.011	0.007	0.008	0.007	0.005	0.012	0.003	0.013	0.003
Si	0.001	0.001	0.002	0.001	0.001	0.002	0.005	0.003	0.000	0.000
Th	0.000	0.000	0.000	0.000	0.000	0.000	0.001	0.000	0.000	0.000
Al	0.000	0.002	0.000	0.000	0.000	0.000	0.004	0.000	0.001	0.001
Y	0.183	0.112	0.173	0.181	0.204	0.181	0.142	0.193	0.172	0.176
La	0.376	0.383	0.377	0.378	0.374	0.373	0.382	0.371	0.382	0.378
Ce	0.001	0.000	0.002	0.000	0.003	0.000	0.000	0.003	0.002	0.001
Pr	0.064	0.080	0.066	0.067	0.058	0.064	0.066	0.063	0.061	0.065
Nd	0.218	0.258	0.223	0.226	0.205	0.225	0.240	0.210	0.222	0.222
Sm	0.045	0.051	0.046	0.046	0.044	0.047	0.049	0.046	0.048	0.048
Eu	0.004	0.007	0.006	0.000	0.005	0.007	0.006	0.003	0.001	0.003
Gd	0.034	0.029	0.035	0.033	0.038	0.035	0.032	0.035	0.036	0.035
Dy	0.023	0.020	0.021	0.022	0.024	0.022	0.021	0.025	0.022	0.023
Ho	0.016	0.017	0.014	0.012	0.013	0.012	0.017	0.015	0.017	0.017
Er	0.001	0.003	0.000	0.001	0.003	0.000	0.003	0.002	0.004	0.003
Tm	0.000	0.000	0.001	0.002	0.001	0.000	0.000	0.000	0.000	0.000
Yb	0.006	0.005	0.004	0.000	0.000	0.002	0.002	0.002	0.002	0.003
Ca	0.019	0.019	0.020	0.020	0.017	0.020	0.019	0.024	0.017	0.020
Fe	0.000	0.001	0.001	0.002	0.003	0.001	0.000	0.000	0.000	0.000
K	0.000	0.001	0.000	0.000	0.000	0.002	0.000	0.001	0.000	0.000
F	0.617	0.615	0.576	0.666	0.548	0.620	0.891	0.534	0.520	0.602
C	1.001	1.000	1.001	1.001	1.002	1.004	0.998	1.004	0.998	1.004
H	0.383	0.385	0.424	0.334	0.452	0.380	0.109	0.466	0.480	0.398

825

826 Table 1. Continued

Sample	11	12	13	14	15	16	17	18	19	20
P_2O_5	0.06	0.15	1.38	0.45	0.12	bdl	0.03	0.04	0.06	0.35
SiO_2	0.04	0.07	0.08	0.03	0.51	bdl	0.04	0.05	0.03	0.07
ThO_2	bdl	0.05	bdl	bdl	bdl	bdl	bdl	bdl	bdl	bdl
Al_2O_3	bdl	0.04	bdl	0.01	0.06	bdl	0.01	bdl	bdl	0.02
Y_2O_3	10.21	7.45	12.92	9.85	10.73	8.10	8.07	8.55	8.60	8.49
La_2O_3	29.14	29.16	27.82	30.62	29.50	29.06	29.88	29.20	29.34	30.39
Ce_2O_3	0.07	0.04	bdl	bdl	bdl	0.01	bdl	bdl	bdl	bdl
Pr_2O_3	5.06	5.60	4.69	5.05	5.05	5.61	5.51	5.33	5.40	5.65
Nd_2O_3	17.82	20.02	16.10	18.31	17.48	19.68	20.05	20.25	19.46	19.13
Sm_2O_3	3.81	4.50	3.19	3.96	3.80	4.23	4.37	4.36	4.27	4.16
Eu_2O_3	0.25	0.24	0.02	0.56	0.28	0.68	0.52	0.73	0.71	0.49
Gd_2O_3	3.26	2.92	3.01	3.14	2.76	2.93	2.77	2.65	3.03	2.59
Dy_2O_3	2.10	1.73	2.36	2.05	2.43	1.89	1.87	1.81	1.95	1.84
Ho_2O_3	1.59	1.14	1.85	1.07	1.38	1.17	1.48	1.48	1.35	1.07
Er_2O_3	0.14	0.26	0.37	0.14	0.31	0.25	0.23	0.07	0.14	0.17
Tm_2O_3	bdl	bdl	bdl	bdl	bdl	bdl	bdl	bdl	bdl	bdl
Yb_2O_3	0.36	0.19	0.62	0.22	0.14	0.39	0.39	0.02	0.41	0.30
CaO	0.54	0.51	0.49	0.55	0.65	0.57	0.63	0.54	0.60	0.59
FeO	bdl	bdl	0.01	0.03	0.06	0.04	0.01	0.06	bdl	bdl
K_2O	0.01	0.03	0.01	0.02	0.17	0.01	0.01	0.01	bdl	0.01
F	5.71	5.87	5.51	5.09	5.32	5.19	5.51	5.85	5.54	6.13
CO_2	21.26	20.87	21.74	21.72	22.06	21.07	21.44	21.29	21.32	21.38
H_2O	1.63	1.48	1.91	2.04	1.98	1.83	1.75	1.56	1.72	1.47
O=F	-2.41	-2.47	-2.32	-2.14	-2.24	-2.18	-2.32	-2.46	-2.33	-2.58
Total	100.65	99.85	101.76	102.77	102.55	100.53	102.25	101.39	101.60	101.72
Formulae based on 1 cation										
P	0.002	0.004	0.039	0.013	0.003	0.000	0.001	0.001	0.002	0.010
Si	0.001	0.002	0.003	0.001	0.017	0.000	0.001	0.002	0.001	0.002
Th	0.000	0.000	0.000	0.000	0.000	0.000	0.000	0.000	0.000	0.000
Al	0.000	0.002	0.000	0.000	0.002	0.000	0.000	0.000	0.000	0.001
Y	0.188	0.139	0.228	0.177	0.190	0.151	0.147	0.157	0.158	0.155
La	0.372	0.378	0.340	0.380	0.363	0.375	0.378	0.372	0.373	0.384
Ce	0.001	0.001	0.000	0.000	0.000	0.000	0.000	0.000	0.000	0.000
Pr	0.064	0.072	0.057	0.062	0.061	0.071	0.069	0.067	0.068	0.071
Nd	0.220	0.252	0.191	0.220	0.208	0.246	0.246	0.250	0.240	0.234
Sm	0.045	0.055	0.036	0.046	0.044	0.051	0.052	0.052	0.051	0.049
Eu	0.003	0.003	0.000	0.006	0.003	0.008	0.006	0.009	0.008	0.006
Gd	0.037	0.034	0.033	0.035	0.030	0.034	0.032	0.030	0.035	0.029
Dy	0.023	0.020	0.025	0.022	0.026	0.021	0.021	0.020	0.022	0.020
Ho	0.017	0.013	0.020	0.011	0.015	0.013	0.016	0.016	0.015	0.012
Er	0.002	0.003	0.004	0.001	0.003	0.003	0.002	0.001	0.002	0.002
Tm	0.000	0.000	0.000	0.000	0.000	0.000	0.000	0.000	0.000	0.000
Yb	0.004	0.002	0.006	0.002	0.001	0.004	0.004	0.000	0.004	0.003
Ca	0.020	0.019	0.017	0.020	0.023	0.021	0.023	0.020	0.022	0.022
Fe	0.000	0.000	0.000	0.001	0.002	0.001	0.000	0.002	0.000	0.000
K	0.000	0.001	0.000	0.001	0.007	0.000	0.000	0.000	0.000	0.000
F	0.625	0.653	0.578	0.542	0.561	0.574	0.598	0.639	0.605	0.664
C	1.004	1.003	0.985	0.999	1.004	1.006	1.005	1.005	1.004	1.000

H	0.375	0.347	0.422	0.458	0.439	0.426	0.402	0.361	0.395	0.336

CO_2 in the mineral is calculated using charge balance method. H_2O is calculated assuming a full (F,OH) site. bdl, below determination limits.

Table 2. Summary of fluid inclusion data from the Zhaibei granites

Inclusion Type	Size (μm)	Tm CO_2 (^oC)	Tm C (^oC)	Th CO_2 (^oC)	Tm	Salinity (wt.%)	Th (^oC)
L_1+L_2+V	8	-58.1	4.2	30.1		10.2	307-L
L_1+L_2+V	5	-57.6	4.1	30.9		10.4	313-L
L_1+L_2+V	7	-57.6	5.7	30.2		7.5	327-L
L_1+L_2+V	7	-57.6	5.1	30.1		8.6	339-L
L_1+L_2+V	9	-57.7	5.8	29.8		7.3	343-L
L_1+L_2+V	8	-58.3	8.2	28.1		3.2	349-G
L_1+L_2+V	9	-57.2	5.2	29.7		8.4	356-L
L_1+L_2+V	8	-57.8	4.9	30.5		9.0	356-L
L_1+L_2+V	7	-57.5	5.4	28.9		8.0	361-L
L_1+L_2+V	8	-57.4	3.5	30.7		11.6	362-G
L_1+L_2+V	6	-58.2	6.3	30.2		6.4	362-L
L_1+L_2+V	8	-58.2	4.9	30.1		9.0	372-L
L_1+L_2+V	9	-58.2	7.9	28.5		3.8	386-G
L+V	7				-7.3	10.9	168
L+V	9				-5.6	8.7	174
L+V	11				-6.3	9.6	182
L+V	9				-4.9	7.7	210
L+V	8				-4.8	7.6	211
L+V	14				-6.4	9.7	218
L+V	5				-5.9	9.1	220
L+V	6				-6.4	9.7	253
L+V	5				-6.1	9.3	276
L+V	10				-5.4	8.4	313
L+V	7				-5.3	8.3	326
L+V	6				-4.8	7.6	345
L+V	9				-5.8	8.9	347

CO_2 melting temperatures (Tm CO_2); Clathrate melting temperatures (Tm C); Partial homogenization temperatures (Th CO_2); ice-melting temperatures (Tm); homogenization temperatures (Th); The letter behind homogenization temperature represents the form of homogenization: L = homogenize to the liquid, G = homogenize to the gas.